Two-photon excited microscale colour centre patterns in Ag-activated phosphate glass written using a focused proton beam

著者	Kurobori Toshio, Kada Wataru, Shirao Taichi, Satoh Takahiro
著者別表示	黒堀 利夫

journal or publication title	Japanese Journal of Applied Physics
volume	57
number	2
page range	02CC01
year	2018-02
URL	http://doi.org/10.24517/00050457

doi: 10.7567/JJAP.57.02CC01

Two-photon excited microscale colour centre patterns in Ag-activated phosphate glass written using a focused proton beam

Toshio Kurobori[1]*, Wataru Kada[2], Taichi Shirao[3], and Takahiro Satoh[4]

[1] *Graduate School of Natural Science and Technology, Kanazawa University, Kanazawa 920-1192, Japan*

[2] *Graduate School of Science and Technology, Gunma University, Kiryu, Gunma 376-8515, Japan*

[3] *Nikon Instech Co., Ltd., Tanakanishi, Kyoto 606-8221, Japan*

[4] *Takasaki Advanced Radiation Research Institute, QST, Takasaki, Gunma 370-1292, Japan*

*E-mail: kurobori@staff.kanazawa-u.ac.jp

We report a demonstration of microscale patterns in Ag-activated phosphate glass fabricated using a focused proton beam with an energy range of 1 – 3 MeV. Various microscale patterns are based on blue and orange radiophotoluminescent (RPL) centres. Two- and three-dimensional (2D and 3D) microstructures are visualised by combining two-photon confocal microscopy with femtosecond (fs) laser pulses generated from a mode-locked Ti:sapphire laser operating at 700 nm. The reconstructed images are analytically evaluated using lateral/axial dose mapping and RPL spectra. In addition, the advantages of two-photon excitation applied to Ag-activated phosphate glass are discussed, and this method is compared with single-photon excitation.

1. Introduction

Micromachining techniques capable of producing sub-microscale structures, including focused ion beam (FIB), proton beam writing (PBW), and ion projection lithography (IPL), have been successfully developed and widely applied in micro-electromechanical systems (MEMS), optoelectronic devices, microfluidic devices, and others.[1,2] The PBW technique, which uses a MeV proton beam focused to small spot sizes, possesses several desirable advantages, such as the fabrication of high-aspect-ratio submicron three-dimensional (3D) structures, the possibility of high penetration depth with little lateral beam spreading, the possibility of controllable penetration depth by varying only the proton beam energy, and the capability of producing structures with high packing density.[3,4] With regard to applications in the field of optoelectronics and microphotonics, a focused MeV light ion (H^+, He^+) beam has been widely applied for functional devices such as waveguides, gratings, microlens arrays formed from poly(methyl methacrylate) (PMMA) photoresists,[5] SU-8 photoresists,[2,6] poly(dimethylsiloxane) (PDMS) film,[7] lithium fluoride (LiF) crystals,[8,9] diamond films,[10] silicon carbide (SiC) films,[11] and noble-ion-doped glasses.[12]

With advances in the aforementioned micromachining techniques, fluorescence light microscopy has been improved to visualise such sub-microscale structures, the dose distribution, and fluorescent spectra written into various materials with higher resolving power. Very recently, we have reported[13] on the demonstration of the nuclear track imaging capabilities of Ag-activated phosphate glass. A cw 375 nm laser and a conventional confocal laser scanning microscope (CLSM) were used for track excitation and detection, respectively. Specifically, the blue and orange radiophotoluminescent (RPL)

tracks and dose distributions observed after irradiation with soft X-rays, gamma rays, and heavy charged particles (HCPs) were examined. Such fluorescent nuclear track detectors (FNTDs) based on Al_2O_3:C,Mg crystals were first developed by Akselrod et al.[14] as one of the most attractive technologies for passive solid-state dosimetry and a novel tool to replace CR-39 plastic nuclear track detectors (PNTDs).[15] Recently, Onoda et al.[16] have successfully observed the ion track using fluorescent nitrogen vacancy (NV) centres in a diamond irradiated with high-energy HCPs via conventional CLSM.

Silver-activated phosphate glass, as described above, is the most widely known RPL material[17-20] and can be used in not only personal, environmental, and clinical dosimeters but also 2D and 3D dose imaging detectors.[21,22] These accumulating passive detectors are based on radiation-induced, optically active, Ag-related atomic-scale centres; therefore, the ultimate intrinsic spatial resolution of these detectors is several nanometres.

In this work, a variety of microscale patterns are written in Ag-activated phosphate glass using a focused proton beam with two different energies, 1.7 and 3 MeV. 2D and 3D microscale patterns are visualised and reconstructed by combining two-photon confocal microscopy with femtosecond (fs) laser pulses generated from a mode-locked Ti:sapphire laser operating at 700 nm. The reconstructed images are analytically evaluated by means of lateral/axial dose distributions and RPL spectra of the microscale pattern based on proton-induced Ag^0 and Ag^{2+} centres. In addition, a significant broadening of the Bragg curve of the experiment in comparison with the simulation is discussed. Finally, advantageous aspects of the two-photon excitation applied to Ag-activated phosphate glass are compared with those of single-photon excitation.

2. Experimental procedure

2.1 Samples

A commercially available Ag-activated phosphate glass plate with dimensions of approximately 8.5 × 8.5 × 1.5 mm^3 was used for the optical measurements and 3D imaging acquisitions. The weight composition of the material used in this study was the same as that of FD-7 (AGC Techno Glass), i.e., 31.55% P, 51.16% O, 6.12% Al, 11.00% Na, and 0.17% Ag. The mass density, photon effective atomic number, and refractive index of this material are 2.61 g/cm^3, 12.57, and 1.52, respectively.

2.2 X-rays

X-ray irradiations were performed using an X-ray unit (RTW, MCB 65C-0, 2x and Spellman, MNX50P50) with a copper (Cu) anode target or a molybdenum (Mo) anode target with the Be window operating at a tube voltage of 40 kV and a current of 1.0 mA and energies of 8 and 17 keV, respectively. The samples were placed at an approximately 10 cm distance from the tube, and the absorbed doses delivered to the samples were 10 Gy.

2.3 Proton beam writing system

The microbeam patterning was performed at the TIARA irradiation facilities of QST Takasaki, Japan.[23)] The proton beam was generated by a single-ended particle accelerator with energies of 1.7 and 3 MeV and then focused to a typical beam size of 1 × 1 μm^2, which was evaluated using a secondary electron image of a copper mesh taken before each irradiation experiment. The irradiation beam current was observed using a beam dump (Faraday cup) connected to a picoamperemeter before and after irradiation. The scanning area of the proton microbeam was controlled using an electrostatic deflection scanner to be a maximum of 800 × 800 μm^2. Proton beams were incident perpendicular to the sample

surface (8.5 × 8.5 mm^2 plane).

Computer-assisted software developed in the laboratory was used to precisely control the irradiated position, exposure time, current, fluence, and repetition of the scanning. The irradiation fluence was in the range of 10^9 - 10^{10} ions/cm^2. Further details of the system are described elsewhere.[10,12, 23)]

2.4 Steady- and transient-state spectra

The steady-state optical absorption spectra (ABS) were determined at RT using a Hitachi U-3900H spectrophotometer with a 1 nm step. The emission (RPL) spectra were recorded at RT using a Hitachi F-2500 fluorescence spectrophotometer. The ionoluminescent spectra were collected with a resolution of 0.5 nm and were corrected for the instrumental calibration.

By comparison, the time-resolved spectra for the blue and orange RPL signals were acquired using a combination of a high-repetition-rate Q-switched laser (Spectra Physics, Explorer One) at 349 nm, a photonic multichannel analyser (Hamamatsu Photonics, PMA-12) and a delay/pulse generator (Stanford Research Systems, DG535). The pulse duration of the laser was less than 5 ns (FWHM) at a repetition rate of 1 kHz for a pulse energy of 1 μJ at the sample. In this work, the blue and orange RPL signals were acquired through a long-pass filter passing all wavelengths larger than 400 nm (Edmund Optics, #84-754). Further details of the system are described elsewhere.[22)]

2.5 Multiphoton confocal microscope

For the observation of a variety of microscale patterns, a multiphoton confocal microscope (Nikon Instech, A1R MP+, hereafter MP+ CLSM) was used. In this work, instead of the 375 nm line emitted from a cw laser diode, fs pulses generated from a Ti:sapphire laser operating at 700 nm as a two-photon excitation source were used to excite the Ag^{2+} and

Ag^0 absorption bands at 350 nm in the Ag-activated glass. The average power output was less than 10 mW at the sample.

For the MP+ CLSM instrument, three objective lenses (Nikon Plan Apo) with different magnifications and numerical apertures (NA) were used: the applied configurations were 20×/0.75NA, 40×/1.15NA/water immersion (refractive index n=1.333), and 100×/1.40NA/oil immersion (n=1.515). The blue RPL signals attributed to Ag^0 centres and the orange RPL signals attributed to Ag^{2+} centres were acquired using a bandpass filter (450 ± 25 nm) and a long-pass filter passing all wavelengths larger than 561 nm, respectively. In addition, the regions of interest (ROI) functions and precisely corrected 32-channel PMT (photomultiplier tube) array detectors with 10 or 6 nm wavelength resolutions were used to investigate the spectral characteristics of the reconstructed microscale patterns in wavelength ranges from 400 to 750 nm or from 439 to 625 nm, respectively.

3. Results and discussion

Figure 1 shows a typical optical absorption (ABS) spectrum including the background (BG, nonirradiation) and normalised emission (RPL) spectrum of Ag-activated glass after X-ray irradiation at an energy of 8 keV with a dose of 10 Gy. The observed absorption features are attributed to the superposition of a number of individual absorption bands in the range from 200 to 700 nm, as previously reported.[18)]

Among them, two bands are dominant: one is the 315 nm absorption band, attributed to the hole-trapped Ag^{2+} centres, and the other is the 350 nm band, attributed to the electron-trapped Ag^0 centres. Exciting the former band results in emission at 630 nm (the

so-called ‘orange RPL’ signal), whereas exciting the latter band results in emission at 450 nm (the so-called ‘blue RPL’ signal).[17-20] Note that the blue and orange RPL signals are simultaneously emitted at single excitation wavelengths ranging from 310 to 380 nm, as indicated in Fig. 1, because of the overlap between the broad absorption bands of the Ag^0 and Ag^{2+} centres. The commercially available laser lines to excite these bands by single-photon excitation are indicated by thin vertical arrows at 337 nm (a pulsed N_2 laser), 349 nm (a Q-switched Nd:YLF laser), 355 nm (3^{rd} harmonics from a Nd:YAG laser), and 375 nm (a cw laser diode). In this work, the 700 nm line generated from a mode-locked Ti:sapphire laser with twice the wavelength of the one-photon absorption of the Ag-activated glass at approximately 350 nm, as indicated by thick vertical arrows, was used to acquire the 2D and 3D fluorescence micro-scale patterns.

From the absorption spectrum in Fig. 1, we estimated the values of the absorption coefficient and attenuation rate at 700 nm (two-photon excitation) and 350 nm (single-photon excitation) when each excitation light propagates a 50 μm length within the X-ray-irradiated sample under a dose of 10 Gy. The absorption coefficients and attenuation rates are 3.3×10^{-4} μm^{-1} and 1.7% at 700 nm and 6.1×10^{-3} μm^{-1} and 30% at 350 nm, respectively. Moreover, as recently reported,[13] 3D fluorescence track images in Ag-activated glass subjected to higher X-ray irradiation at an energy of 8 keV (>30 Gy) could not be collected using conventional single-photon excited CLSM (Nikon Instech, C2 plus) owing to the strong saturation effects of the dense trapping centres produced in the vicinity of the surface. In contrast, in the case of the ^{137}Cs (662 keV) gamma-ray irradiation that delivered a dose of 1 Gy, the absorption coefficients and attenuation rates are 5.1×10^{-5} (μm^{-1}) and 0.3% at 700 nm and 1.4×10^{-4} (μm^{-1}) and 0.7% at 350 nm, respectively.

In addition, the 3D dose distribution was examined via MP+ CLSM using Ag-activated glass irradiated by X-rays at an energy of 17 keV with a dose of 10 Gy. The images were then reconstructed (not shown here) with a field of view of 345.5 × 345.5 μm^2 and a total of 753 layers separated by increments of 0.42 μm at depths ranging from 0 to 318.1 μm below the surface, which were obtained using the 40×/1.15NA/water immersion objective lens. Figure 2 shows a set of dose distribution profiles as a function of the depth from the surface to 318 μm within the sample. These dose profiles, acquired with 32 different wavelengths ranging from 439 to 625 nm with a 6 nm wavelength resolution, were analytically reconstructed from the aforementioned 3D images. Each of the 753 layers (every 0.42 μm pitch) is representative of the corresponding concentrations of proton-induced Ag^0 and Ag^{2+} centres.

The X-ray attenuation length observed from the dose distributions in Ag-activated glass at the X-ray energy of 17 keV has been estimated to be 369 μm using the following parameters (chemical formula: Ag:P_4O_{10}, density: 2.61 g/cm^3)[24], at which the RPL intensity decreases to a factor of e^{-1}=0.368 with respect to its peak value at the surface. This value agrees well with the experimental results. In the case of X-ray irradiation, a photon beam penetrating the material, in general, exhibits an exponentially decreasing dose distribution with penetration depth. The dotted line represents the exponential fitting curve for 625 nm wavelength. As shown in the inset, the rapid attenuation of the RPL intensity of the corresponding 3D image was observed in the vicinity of over approximately 170 μm at depths below the surface. However, the origins of the phenomena are now under consideration.

Figure 3 shows a variety of microscale test patterns, including (a) QR code; (b) lines, circles and dots; (c) squares; and (d) dashed lines, circles, and dots written on the

Ag-activated glass using a focused proton beam with an energy of 1.7 MeV and a current of 4 pA (average value). These 3D patterns, with a 679.5 × 679.5 μm^2 field of view and a total of approximately 30 layers separated by increments of 1.19 μm at depths ranging from 0 to ~40 μm below the surface, were acquired and reconstructed using the MP+ CLSM instrument with a 20×/0.75NA objective lens configuration. Since the projected range (or penetration depth) depends on the beam energy, the 1.7 MeV proton beam used here stopped at the estimated range (~30 μm depth), which was calculated using the SRIM software.[25] In these cases, the total proton exposure times to fabricate such patterns ranged from approximately several seconds to several tens of seconds per pattern.

Figure 4(a) demonstrates a similar 3D pattern written using a focused proton beam with an energy of 1.7 MeV and a current of 20 pA. The 3D patterns, consisting of dots and lines with a 679.5 × 679.5 μm^2 field of view and a total of 35 layers separated by increments of 1.19 μm, were reconstructed with the 20×/0.75NA objective lens configuration. The inset shows a zoomed-in image of the pattern. Note that each dot and line has a different proton exposure time and beam current to evaluate the best conditions.

In these cases of Figs. 3(a)-3(d) and Fig. 4(a), the typical surface spot size was approximately 1×1 μm^2 for the focused proton beam, while in the case of Fig. 4(b), the surface spot size was approximately 3×8 μm^2. Figures 4(c) and 4(d) demonstrate the dot-array images of Fig. 4(b) at fixed depths of 2.21 and 10.46 μm below the surface, respectively, created using a 1.7 MeV proton single shot. In these cases, the blue and orange RPL signals were acquired at wavelengths of 446 and 630 nm, respectively, and each dot image was reconstructed using the 100×/1.40NA/ oil immersion (n=1.515) objective lens [Fig. 4(c)] and additive scan zoom 2× (total magnification, 200×) [Fig. 4(d)] configuration. It was found that the surface spot size of 3×8 μm^2 for the focused proton

beam gradually enlarged from spot sizes of 3.3×8.5 μm^2 at a depth of 2.21 μm to 8.1×10.6 μm^2 at a depth of 10.46 μm.

To investigate the spectral characteristics of the reconstructed microscale patterns written using a focused proton beam with an energy of 3 MeV and a current of 20 pA, a limited field of area (ROI#1, 160×140 pixels) was selected using the ROI functions in the NIS-Elements software, as shown in Fig. 5(a). Figure 5(b) shows the corresponding spectrum of the ROI#1 area, which was obtained using a 32-channel PMT array detector with a 10 nm-wavelength resolution in the range from 400 to 750 nm. The inset shows a photograph of the microscale patterns used in the work, 680 × 680 μm^2 in area, created in the Ag-activated glass with dimensions of 8.5 × 8.5 × 1.5 mm^3. An intense orange RPL luminescence under excitation with UV light was observed with the naked eye. To directly record the RPL spectrum of the microscale pattern of this sample, the time-resolved spectra were also examined. Both RPL spectra fairly agree with those measured using a conventional fluorescence spectrophotometer, as shown in Fig. 1.

Figure 6(a) shows a typical 2D image of the dot pattern written using a single-shot proton beam with a total of 35 image layers separated by increments of 1.19 μm at depths ranging from 0 to 41.8 μm below the surface, as shown in Fig. 4(a). Two ROIs (ROI#1 and ROI#2) were set in the constructed image, one for signal (ROI#1) and the other for background (ROI#2). Note that the background value of each 1.19 μm depth was subtracted from each RPL signal. Figure 6(b) presents the RPL intensity profile along the axial direction perpendicular to the surface obtained by the image analysis method for orange and blue RPL. Normalised SRIM-simulated energy loss profiles are also presented as inserts. The calculated profile (dashed lines) indicates that the energy loss through the ionisation and excitation of atoms increases slowly with depth and increases rapidly only at

the end of range (Bragg peak), where the energy loss due to proton/nuclear collisions increases. The estimated distance between the surface and the peak intensity of the luminescence profile was approximately 30 μm. This value is in good agreement with the Bragg peak position of 30.2 μm obtained by the SRIM software[25] for protons of 1.7 MeV energy.

Similar processes were also applied to other patterns. Figures 7(a) and 7(b) show 2D images of the square pattern with a total of 35 image layers separated by increments of 1.19 μm [Fig. 7(a)] and a total of 47 image layers separated by increments of 2.39 μm [Fig. 7(b)], which were written using multiple-shot proton beams with energies of 1.7 and 3 MeV, respectively. As described above, two ROIs (ROI#1 and ROI#2) were set, and then each background value (ROI#2) was subtracted from that of the RPL signal (ROI#1). Figures 7(c) and 7(d) show the corresponding RPL intensity profiles along the axial direction for the orange and blue RPL signals, respectively. The estimated distances between the surfaces and the peak intensity of the luminescence profile along the depths were in good agreement with the Bragg peak positions for protons of 1.7 and 3 MeV energies, which are 30.2 and 75.5 μm, respectively. Remarkably, in this case, the RPL intensity saturation for 1.7 MeV was observed from the initial depth of approximately 15 μm to the penetration depth due to multiple-shot irradiations, as shown in Fig. 7(c).

However, as shown in Fig. 6(b), even in single-shot irradiations, a significant broadening of the Bragg curve in the experiment was observed compared with the simulation, likely because the proton beam used in this work generally travels in a straight line, apart from a small amount of end-of-range broadening, a behaviour that is quite different from that in e-beam writing and FIB writing, which use low-energy heavy ions.

In the case of PMMA, it has been reported that the lateral beam broadening is only 2 μm at the end of range for 2 MeV protons[2)] and the penetration depth in PMMA is 60.8 μm. The result suggests that beam broadening strongly depends on the composition of the material and its atomic network within the host.

Furthermore, such broadening effects are probably caused by the lack of depth resolution of the MP+ CLSM. In this work, the observation and reconstruction of 2D and 3D images were carried out via MP+ CLSM. However, the image resolution obtained with two-photon excitation may not be better than that achieved with a conventional confocal microscope with the use of a confocal pinhole to reject out-of-focus background.[26)] Although a larger excitation wavelength (at 700 nm) is an advantageous aspect of two-photon excitation, it actually results in a larger resolution spot compared with single-photon excitation (at 350 nm). Therefore, the lateral/axial resolution of a MP+ CLSM is almost equal to that of a conventional CLSM in the case of Ag-activated glass: the approximate lateral (x, y) resolution is in the range of 180 – 250 nm, while the axial (z) resolution is in the range of 500 – 700 nm under visible light.[27)]

However, these results suggest that two-photon excitation microscopy is more effective than single-photon excitation microscopy[26)] for Ag-activated glass: the lack of out-of-focus absorption allows for more of the excitation light to reach the desired sample region. Two-photon excitation provides an advantage for thick samples and/or samples with high concentrations (e.g., X-rays) of induced-active luminescent centres close to the surface; the larger (such as red or near-NIR) wavelengths are scattered less than the smaller (such as UV or blue) wavelengths. In this work, 350 nm (single-photon) light would be expected to undergo approximately sixteenfold more scattering than 700 nm (two-photon) light, as predicted by an approximation of Rayleigh scattering. The effects of fluorescence

scattering are less detrimental to two-photon microscopy than to conventional confocal microscopy. Additionally, the damage and photobleaching caused by UV light with a higher photon energy would be more significant, especially for biological applications in brain research, neuroscience, and in vivo imaging of living cells and tissues.

4. Conclusions

The data obtained in this study led to the following conclusions:

(1) A variety of microscale patterns in Ag-activated phosphate glasses written using focused high-energy light ions (proton) were demonstrated and evaluated utilising two-photon confocal microscopy for the first time.

(2) The dose distributions as a function of the implantation depth for single-shot and multiple-shot proton beams were measured, and a significant broadening of the Bragg curve in the experiment when compared with the simulation was discussed.

(3) The X-ray attenuation length within Ag-activated glass was measured utilising 32 different wavelengths from 439 to 625 nm, and the profiles, estimated to be 369 μm for the X-ray energy of 17 keV, were in good agreement with the calculations.

(4) The axial resolution of the two-photon excited microscope when applied to Ag-activated phosphate glass was compared with that of the single-photon excited confocal microscope.

Acknowledgements

T. K would like to thank Professor H. Nanto at the Kanazawa Institute of Technology for valuable discussions, and Y. Yanagida, Y. Koguchi, N. Takeuchi, Professor T. Yamamoto,

and the staff of Chiyoda Technol Corporation for their contributions in the form of insightful discussions and sample preparation. This work was supported by JSPS KAKENHI Grant Number 17H03519.

References

1) F. Watt, Nucl. Instrum. Methods Phys. Res., Sect. B **158**, 165 (1999).
2) F. Watt, A. A. Bettiol, J. A. van Kan, E. J. Teo, and M. B. H. Breese, Int. J. Nanosci. **4**, 269 (2005).
3) F. Watt, M. B. H. Breese, A. A. Bettiol, and J. A. van Kan, Mater. Today **10**, 20 (2007).
4) T. Kamia, K. Takano, Y. Ishii, T. Satoh, M. Oikawa, T. Ohkubo, J. Haga, H. Nishikawa, Y. Furuta, N. Uchiya, S. Seki, and M. Sugimoto, Nucl. Instrum. Methods Phys. Res., Sect. B **267**, 2317 (2009).
5) J. A. van Kan, A. A. Bettiol, and F. Watt, Appl. Phys. Lett. **83**, 1629 (2003).
6) N. Uchiya, T. Harada, M. Murai, H. Nishikawa, J. Haga, T. Sato, Y. Ishii, and T. Kamiya, Nucl. Instrum. Methods Phys. Res., Sect. B **260**, 405 (2007).
7) W. Kada, K. Miura, H. Kato, S. Saruya, A. Kubota, T. Satoh, M. Koka, Y. Ishii, T. Kamiya, H. Nishikawa, and O. Hanaizumi, Nucl. Instrum. Methods Phys. Res., Sect. B **348**, 218 (2015).
8) M. Cremona, J. A. M. Pereira, S. Pelli, and G. C. Righini, Appl. Phys. Lett. **81**, 4103 (2002).
9) V. Mussi, F. Somma, P. Moretti, J. Mugnier, B. Jacquier, R. M. Montereali, and E. Nichelatti, Appl. Phys. Lett. **82**, 3886 (2003).
10) W. Kada, A. Yokoyama, M. Koka, K. Takano, T. Satoh, and T. Kamiya, Jpn. J. Appl. Phys. **51**, 06FB07 (2012).
11) H. Kraus, D. Simin, C. Kasper, Y. Suda, S. Kawabata, W. Kada, T. Honda, Y. Hijikata, T. Ohshima, V. Dyakonov, and G. V. Astakhov, Nano Lett. **17**, 2865 (2017).
12) S. Kawabata, W. Kada, R. K. Parajuli, Y. Matsubara, M. Sakai, K. Miura, T. Satoh, M. Koka, N. Yamada, T. Kamiya, and O. Hanaizumi, Jpn. J. Appl. Phys. **55**, 06GD03 (2016).
13) T. Kurobori, Y. Yanagida, S. Kodaira, and T. Shirao, Nucl. Instrum. Methods Phys. Res., Sect. A **855**, 25 (2017).
14) G. M. Akselrod, M. S. Akselrod, E. R. Benton, and N. Yasuda, Nucl. Instrum. Methods Phys. Res., Sect. B **247**, 295 (2006).
15) B. G. Cartwright, E. K. Sirk, and P. B. Price, Nucl. Instrum. Methods. Res., Sect. **153**, 457 (1978).

16) S. Onoda, M. Haruyama, T. Teraji, J. Isoya, W. Kada, O. Hanaizumi, and T. Ohshima, Phys. Status Solidi A **212**, 2641 (2015).
17) J. A. Perry, *RPL Dosimetry, Radiophotoluminescence in Health Physics* (Adam Hilger, Bristol, 1987).
18) T. Kurobori, W. Zheng, Y. Miyamoto, H. Nanto, and T. Yamamoto, Opt. Mater. **32**, 1231 (2010).
19) Y. Miyamoto, Y. Takei, H. Nanto, T. Kurobori, A. Konnai, T. Yanagida, A. Yoshikawa, Y. Shimotsuma, M. Sakakura, K. Miura, K. , Y. Nagashima, and T. Yamamoto, Radiat. Meas. **46**, 1480 (2011).
20) http://www.c-technol.co.jp/eng/e-p_monitoring
21) T. Kurobori and S. Nakamura, Radiat. Meas. **47**, 1009 (2012).
22) T. Kurobori, Y. Yanagida, and Y. Q. Chen, Jpn. J. Appl. Phys. **55**, 02BC01 (2016).
23) T. Kamiya, T. Satoh, M. Koka, and W. Kada, Nucl. Instrum. Methods Phys. Res., Sect. B **348**, 4 (2015).
24) http://henke.lbl.gov/optical_constants/atten2.html
25) J. F. Ziegler, M.D. Ziegler, J. P. Biersack, Nucl. Instrum. Methods Phys. Res., Sect. B **268**, 1818 (2010).
26) https://www.microscopyu.com/techniques/multi-photon/multiphoton-microscopy
27) L. Schermelleh, R. Heintzmann, and H. Leonhardt, J. Cell. Biol. **190**, 165 (2010).

Figure Captions

Fig. 1. (Colour online) Typical optical spectra of Ag-activated glass after X-ray irradiation at an energy of 8 keV with a dose of 10 Gy. (left) Absorption (ABS) spectrum including background (BG) and (right) emission (RPL) spectrum. The thin and thick vertical arrows represent the available single-photon laser lines and two-photon laser lines to excite the absorption band, respectively.

Fig. 2. (Colour online) A set of RPL dose distribution profiles as a function of the depth from the surface to 318 μm within the sample after X-ray irradiation at an energy of 17 keV. Depth profiles of the RPL intensity obtained from various wavelengths from 439 to 625 nm with a 6-nm-wavelength resolution. The dotted line shows the exponential fitting curve for 625 nm wavelength. The inset shows a picture of the corresponding 3D image.

Fig. 3. (Colour online) Observation of a variety of microscale patterns via MP+ CLSM in Ag-activated glass written using a focused proton beam with an energy of 1.7 MeV and a current of 4 pA. (a) QR code, (b) lines, circles and dots, (c) squares, and (d) dashed lines, circles, and dots.

Fig. 4. (Colour online) Observation of a microscale pattern via MP+ CLSM in Ag-activated glass written using a focused proton beam with an energy of 1.7 MeV and a current of 20 pA. 3D images of the dots and lines pattern and a zoomed-in image for the case with the surface spot sizes of (a) 1×1 and (b) 3×8 μm^2. Magnified dot-array images at depths of (c) 2.21 and (d) 10.46 μm in Fig. 4(b), detected with wavelengths of 446 nm for blue RPL and 630 nm for orange RPL.

Fig. 5. (Colour online) (a) Microscale pattern written using a proton beam with an energy of 3 MeV and setting position of ROI#1. (b) Corresponding RPL spectra recorded using an MP+ CLSM system and time-resolved instrument. The inset shows a photograph of the microscale pattern directly written within the sample.

Fig. 6. (Colour online) (a) 2D image of the dot pattern written by single-shot proton beam

irradiation with an energy of 1.7 MeV and setting position of two ROIs. (b) Corresponding dose distribution profiles as a function of depth from the surface for orange and blue RPL and the normalised SRIM simulations.

Fig. 7. (Colour online) 2D images of the square pattern written by multiple-shot proton beam irradiation with energies of (a) 1.7 and (b) 3.0 MeV and setting position of two ROIs. Corresponding dose distribution profiles as a function of depth from the surface for orange and blue RPL at energies of (c) 1.7 and (d) 3.0 MeV.

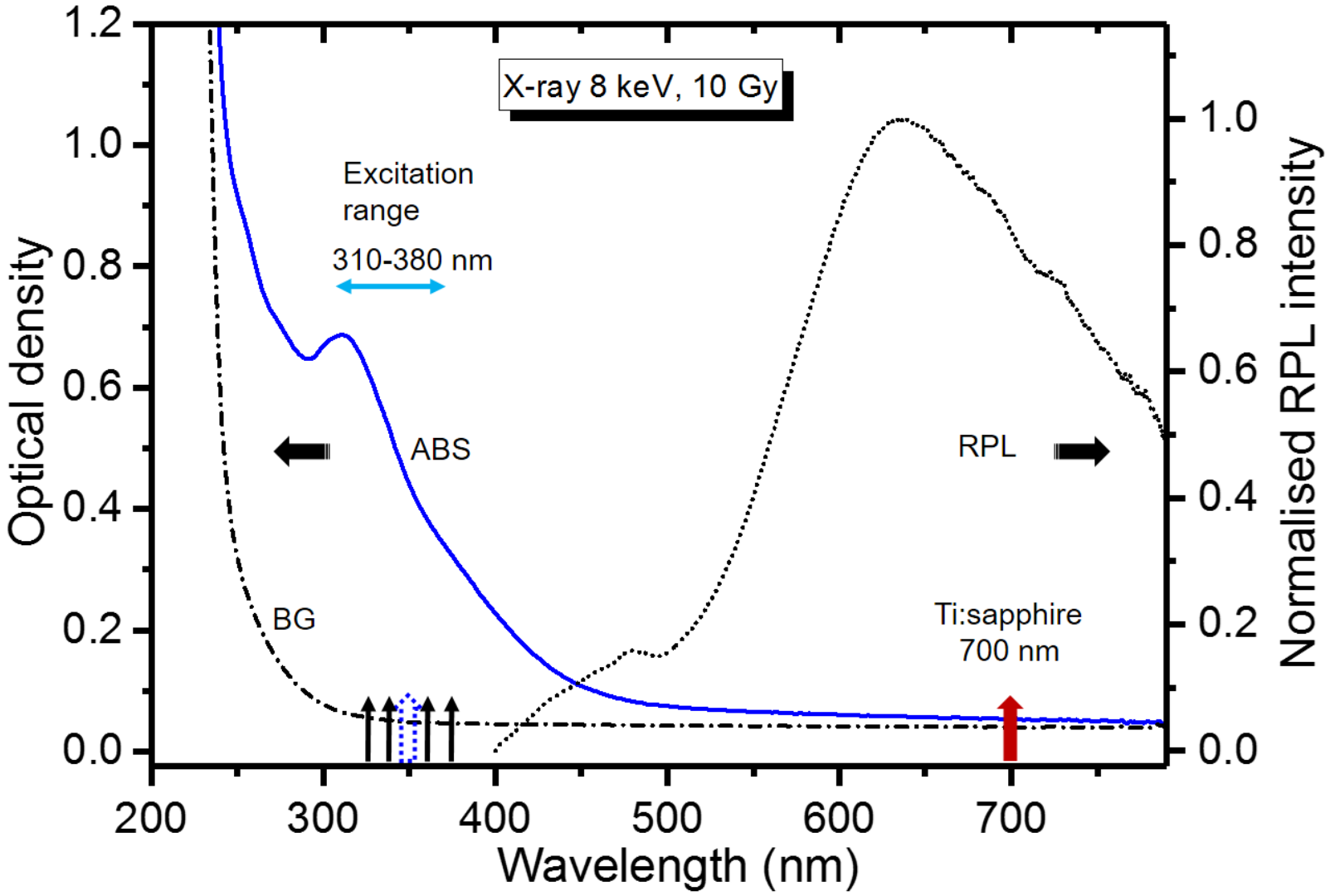

(Colour Online) EM17011Fig1

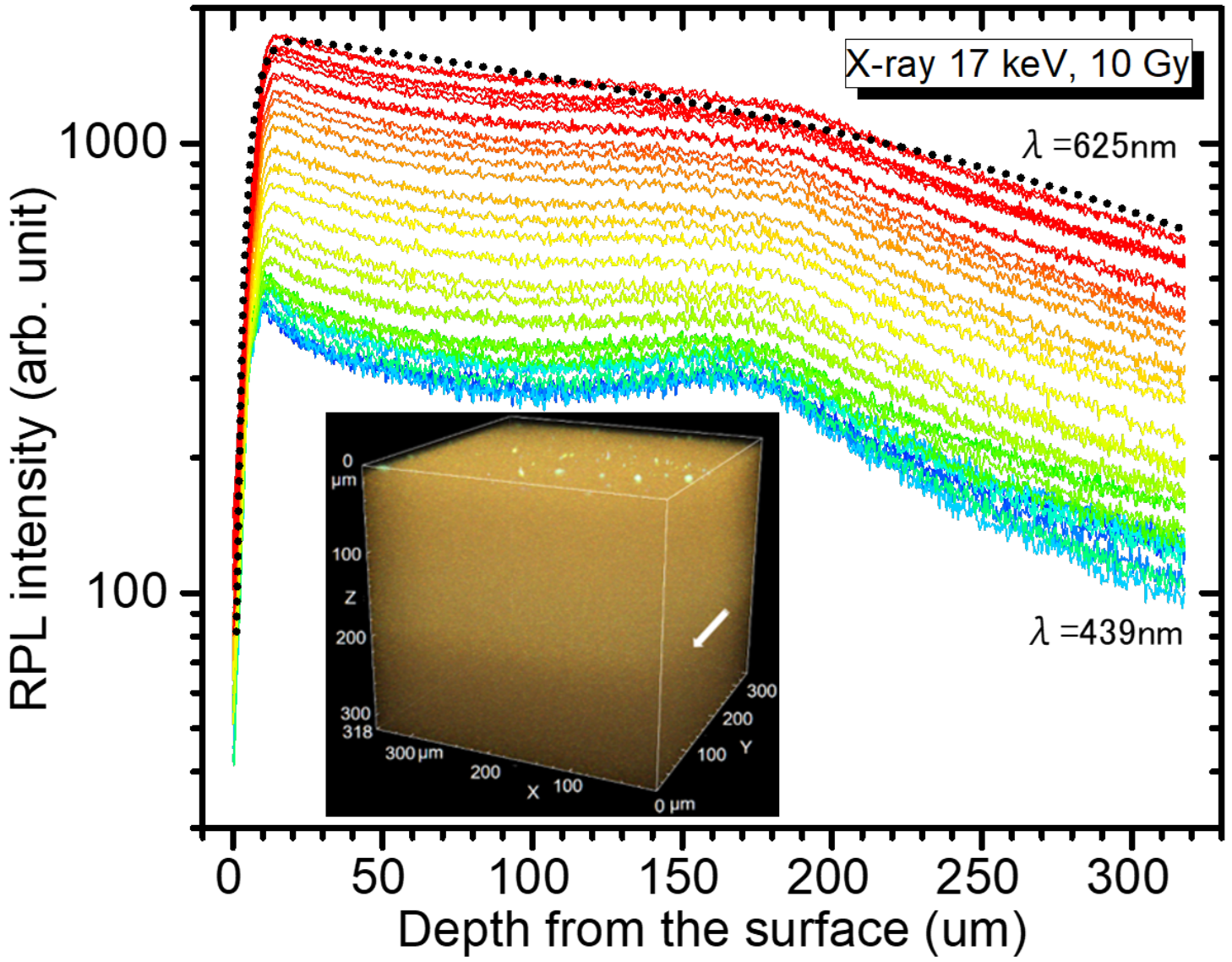

(Colour Online) EM17011 Fig2

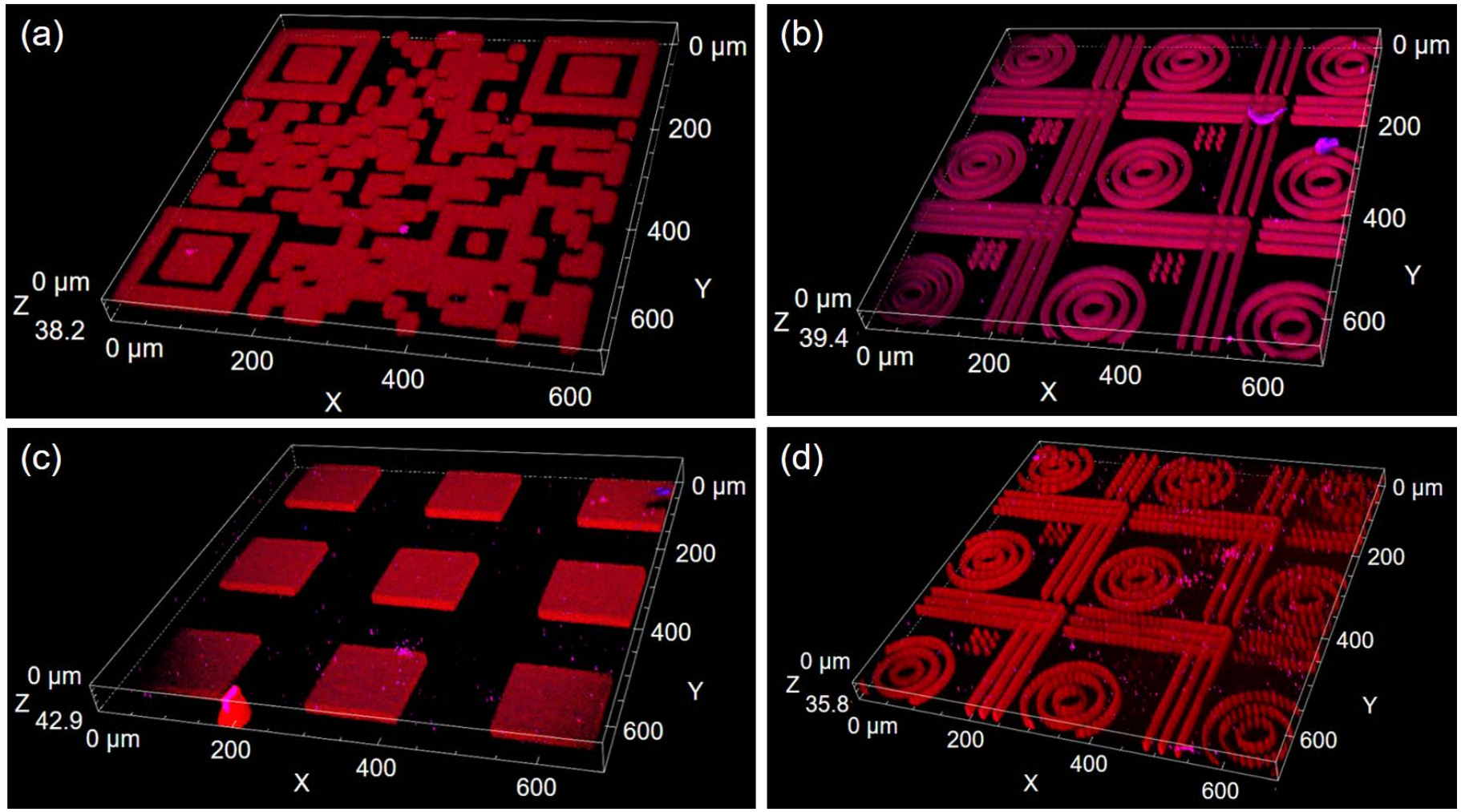

(Colour Online) EM17011Fig3

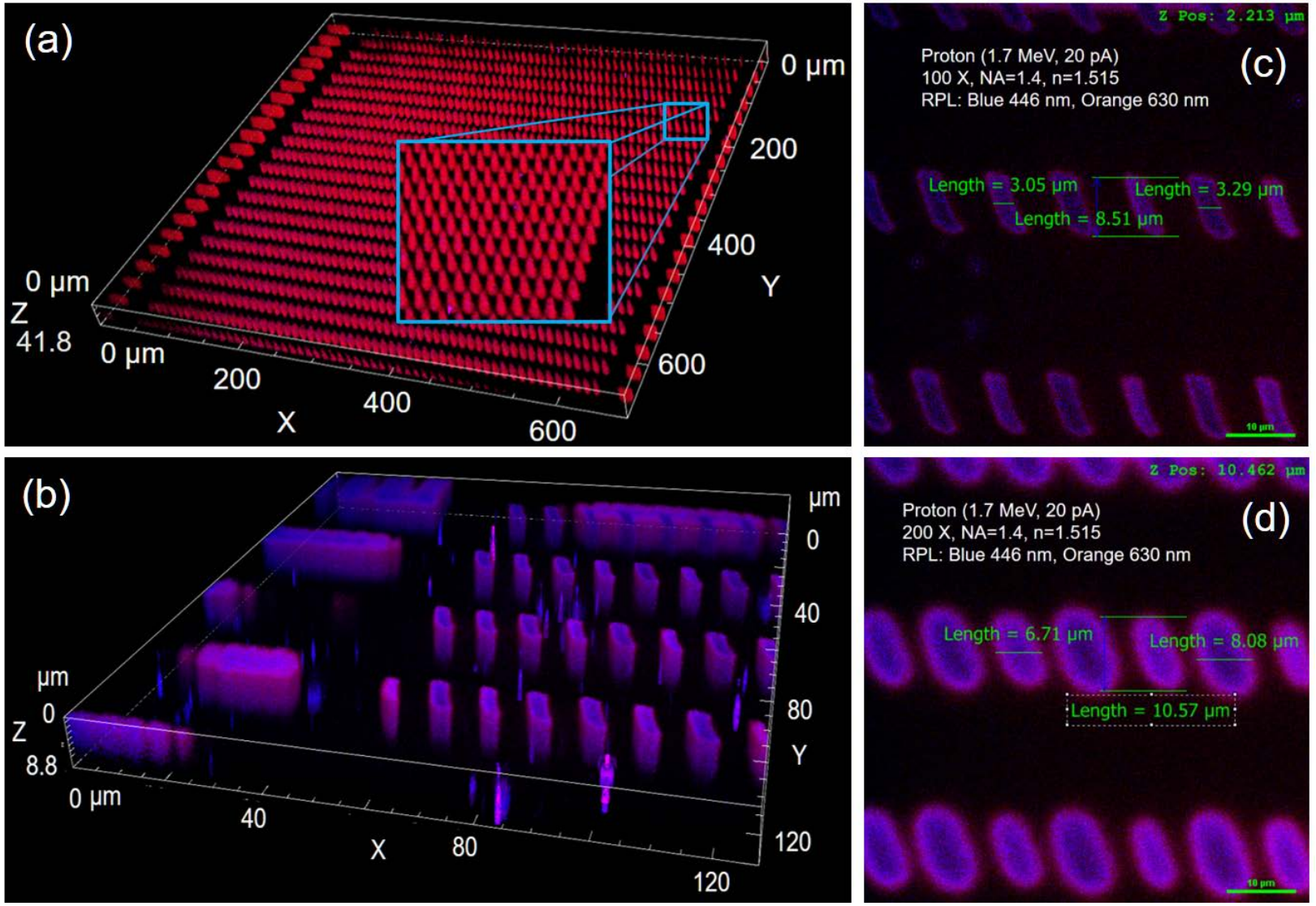

(Colour Online) EM17011Fig4

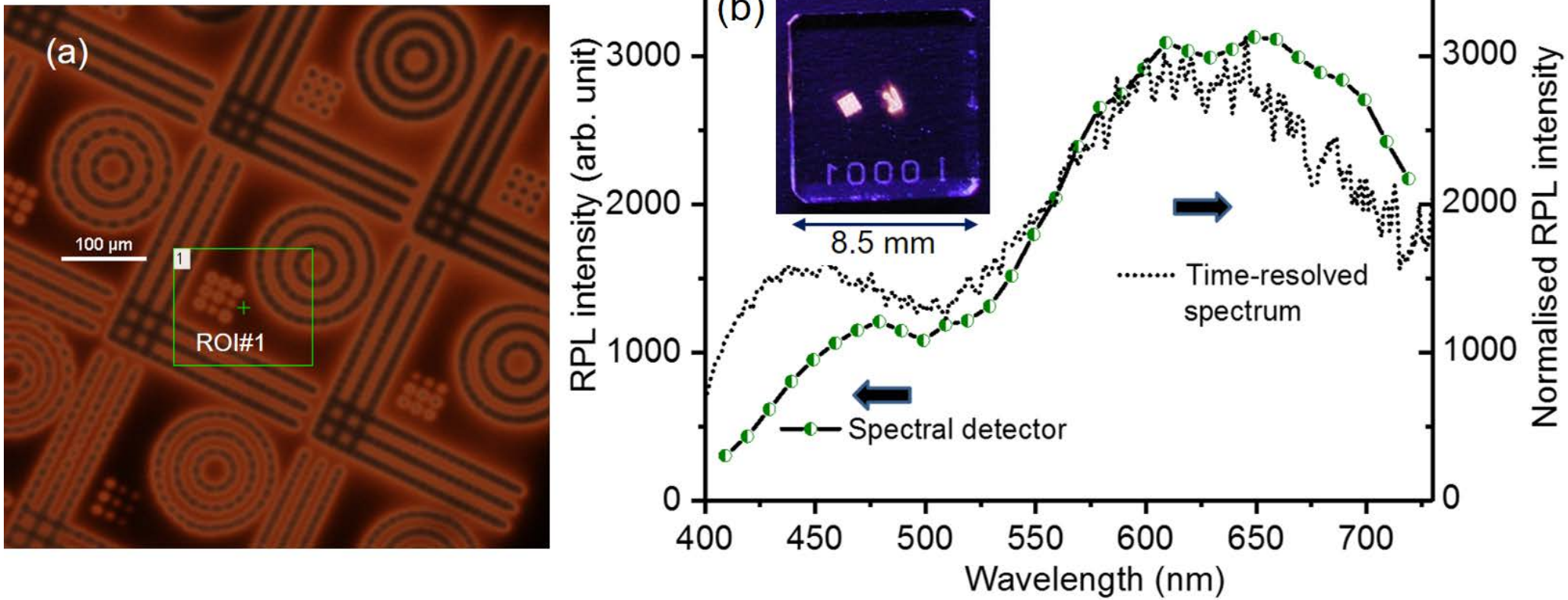

(Colour Online) EM17011Fig5

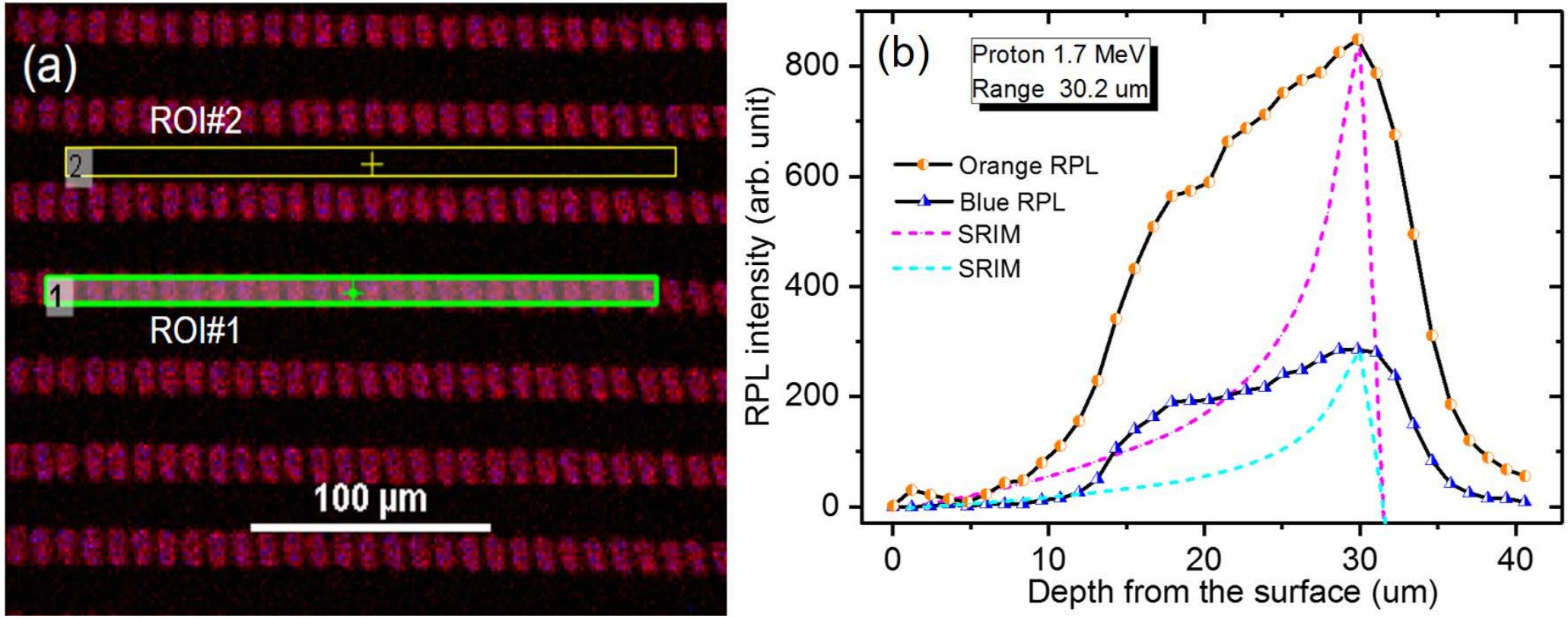

(Colour Online) EM17011Fig6

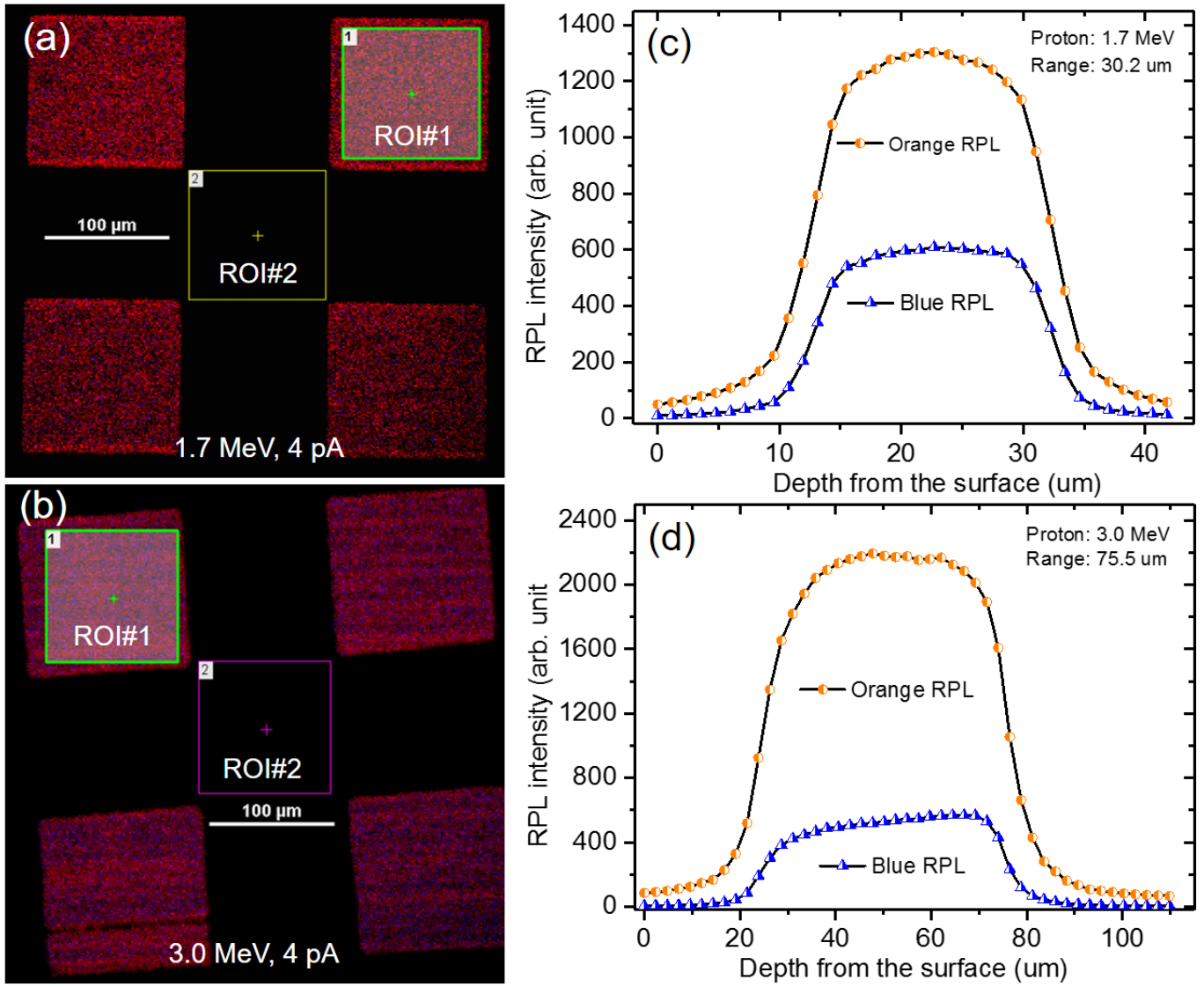

(Colour Online) EM17011Fig7